This is the Pre-Published Version.

This document is the Accepted Manuscript version of a Published Work that appeared in final form in Journal of the American Chemical Society, copyright © American Chemical Society after peer review and technical editing by the publisher. To access the final edited and published work see https://dx.doi.org/10.1021/jacs.1c06877.

Journal of the American Chemical Society is available at https://pubs.acs.org/journal/jacsat.

A new hexagonal cobalt nanosheet catalyst for selective CO_2 conversion to ethanal

Jie Yin[†,⊥,#], Zhouyang Yin[†,#], Jing Jin[⊥,#], Mingzi Sun[‡], Bolong Huang[‡,*], Honghong Lin[†], Zhenhui Ma[†], Michelle Muzzio[†], Mengqi Shen[†], Chao Yu[†], Hong Zhang[&], Yong Peng[&], Pinxian Xi[⊥,*], Chun-Hua Yan[⊥,‖], Shouheng Sun[†,*]

[†]Department of Chemistry, Brown University, Providence, Rhode Island 02912, United States.

[⊥]State Key Laboratory of Applied Organic Chemistry, Frontiers Science Center for Rare Isotopes, Key Laboratory of Nonferrous Metal Chemistry and Resources Utilization of Gansu Province, College of Chemistry and Chemical Engineering, Lanzhou University, Lanzhou 730000, China.

[‡]Department of Applied Biology and Chemical Technology, The Hong Kong Polytechnic University, Hung Hum, Kowloon, Hong Kong SAR, China.

[&]Key Laboratory of Magnetism and Magnetic Materials of Ministry of Education, School of Physical Science and Technology, Lanzhou University, Lanzhou 730000, China.

[‖]Beijing National Laboratory for Molecular Sciences, State Key Laboratory of Rare Earth Materials Chemistry and Applications, PKU-HKU Joint Laboratory in Rare Earth Materials and Bioinorganic Chemistry, College of Chemistry and Molecular Engineering, Peking University, Beijing 100871, China.

KEYWORDS: Metallic nanosheets, hcp-Co, CO_2 reduction, electrocatalysis, ethanal formation

ABSTRACT: We report a new form of catalyst based on ferromagnetic hexagonal-close-packed (*hcp*) Co nanosheets (NSs) for selective CO_2RR to ethanal, CH_3CHO. In all reduction potentials tested from -0.2 to -1.0 V (vs. RHE) in 0.5 M $KHCO_3$ solution, the reduction yields ethanal as a major product and ethanol/methanol as minor products. At -0.4 V, the Faradaic efficiency (FE) for ethanal reaches 60% with current densities of 5.1 mA cm^{-2} and mass activity of 3.4 A g^{-1} (total FE for ethanal/ethanol/methanol is 82%). Density functional theory (DFT) calculations suggest that this high CO_2RR selectivity to ethanal on the *hcp* Co surface is attributed to the unique intra-layer electron transfer, which not only promotes [OC-CO]* coupling but also suppresses the complete hydrogenation of the coupling intermediates to ethylene, leading to highly selective formation of CH_3CHO.

INTRODUCTION:

Carbon dioxide (CO_2) reduction reaction (CO_2RR) to value-added chemicals and fuels is an essential step required to achieve green and sustainable chemistry/energy.[1–5] Electrochemical CO_2RR under ambient conditions has been studied extensively as a promising approach to selective CO_2RR.[6–8] Various electrocatalysts have been designed and tested for the CO_2RR, and those leading to selective CO_2 conversion to carbon monoxide (CO)[9–12] or formate ($HCOO^-$)[13–17] have been demonstrated. However, selective CO_2RR *via* carbon-carbon (C-C) coupling to a specific hydrocarbon product is extremely challenging due to the multiple pathways involved in the reaction process,[18–22] and Cu-based catalysts have been the universal choice to build the C-C structure in electrochemical CO_2RR.[23–27] Up to now, the most widely reported Cu-catalyzed CO_2RR is the formation of ethylene[28–30] along with other products,[31–34] including oxygenated hydrocarbons,[35–38] but selective formation to aldehyde (RCHO) has rarely been reported.[39,40]

Here we report a new catalyst based on ferromagnetic Co nanosheets (NSs) for selective electrochemical reduction of CO_2 to ethanal, CH_3CHO. These Co NSs have a hexagonal-close-packed (*hcp*) structure and are ferromagnetic at room temperature. They are also thermally stable and can only be converted to face centered cubic (*fcc*) structure at 900 °C. Under electrochemical reduction conditions, the *hcp* Co NSs catalyze the CO_2RR to ethanal as the major product and ethanol (CH_3CH_2OH) and methanol (CH_3OH) as minor products (the *fcc* Co NSs are much less active and selective). At -0.4 V *vs*. reversible hydrogen electrode (RHE), the Faradaic efficiency (FE) for ethanal reaches 60% (total FE for ethanal, ethanol, and methanol is 82%). Density functional theory (DFT) calculations suggest that the *hcp* and *fcc* Co NSs have intrinsic electroactivity differences that arise from the intra-layer electron transfer capability and surface oscillation strength. CO_2 is more favorably adsorbed and activated on the *hcp* Co NS surface than on the *fcc* Co NS surface *via* the intra-layer electron transfer, which directs the CO_2RR to follow the selective C_2 pathway, achieving a controlled reduction of C_2 intermediates to ethanal. This *hcp* Co NS catalyzed CO_2RR offers a new direction in designing transition metal catalysts for active and selective CO_2RR.

RESULTS AND DISCUSSION:

Material Synthesis and Characterizations. The *hcp* Co NSs were prepared by exfoliation (in formamide) of the aggregated Co NSs obtained from hydrothermal reaction of $CoCl_2$ and hydrazine at 160 °C for 5 h (see details in supporting information (SI), and **Figure S1**). The as-synthesized Co NSs were dispersible in either formamide or ethanol. The separated Co NSs were first characterized by thermal gravimetric analysis (TGA) under N_2 atmosphere from 30 to 500 ºC. **Figure S2** shows the TGA results for the Co NS samples before and after the formamide exfoliation treatment. Neither the aggregated Co sample nor the *hcp* Co NS sample shows an obvious mass drop below 200 ºC, and both of them demonstrate their ability of adsorbing N_2 above 238.6 ºC (for the *hcp* Co NSs), and 285.3 ºC (for the aggregated Co sample), which suggest that the Co surface is organics-free. X-ray diffraction (XRD) of the NSs (**Figure 1a**) shows a pattern that is consistent with *hcp* Co structure (JCPDS No.1-1278; $P6_3/mmc$; a = b = 2.514 Å; c = 4.105 Å). Transmission electron microscopy (TEM) image (**Figure 1b**) shows that the NS has the two-dimensional sheet morphology. High-angle annular dark field aberration-corrected scanning TEM (HAADF-STEM) provides a view of a fine local structure of the *hcp* Co NS (**Figure 1c**). The corresponding FFT image of STEM (inset in **Figure 1c**) confirms the hexagonal arrangement of Co atoms. The Co element profile (**Figure 1d**) obtained from the scanning along the green line in **Figure 1c** shows an even intensity for the Co-Co distance of 0.25 nm, which is close to the lattice parameter in the *ab* plane of the *hcp* Co lattice. The NS morphology

was further characterized by atomic force microscopy (AFM) (**Figure 1e**). The average thickness of the *hcp* Co NSs was measured to be 1.30 nm (**Figure 1f**), which is equal to the length about 3-unit cells stacking along the crystallographic *c*-direction (for the *hcp* Co unit cell, c = 4.105 Å).

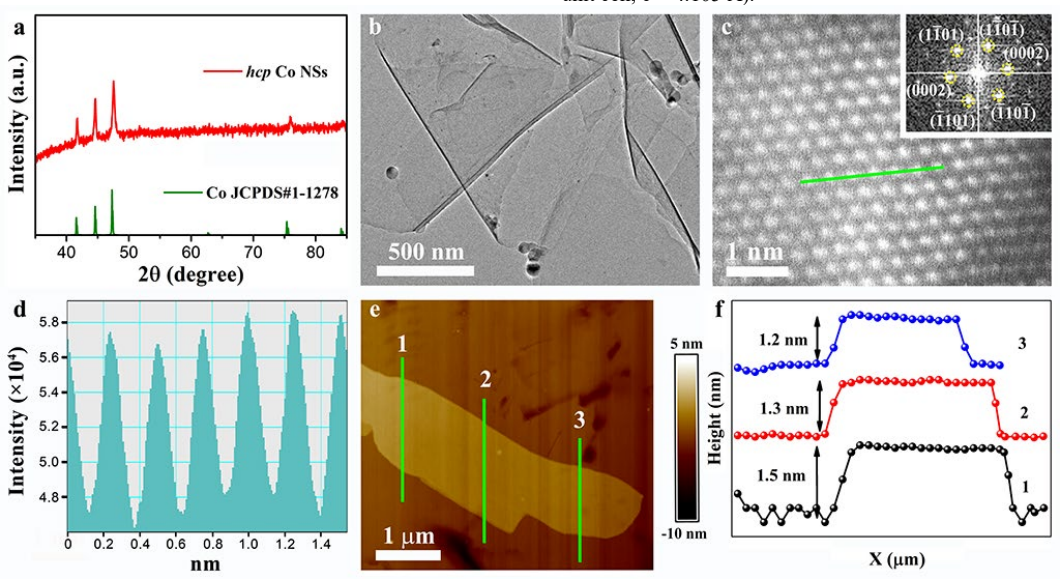

Figure 1. Characterizations of *hcp* Co NSs. (a) Typical XRD pattern of *hcp* Co NSs. (b) TEM image of *hcp* Co NSs. (c) HAADF-STEM image of a local area of the *hcp* Co NS. Inset: Indexed FFT of the area imaged. (d) Co elemental intensity profile obtained from STEM along the green line highlighted in (c). (e) AFM image of a representative piece of *hcp* Co NS, and (f) the corresponding height profiles obtained from three different line scans of 1, 2, 3 in (e).

To further prove that stable metallic NSs are indeed formed from the synthesis, we characterized the electronic, magnetic and chemical oxidation properties of *hcp* Co NSs. X-ray photoelectron spectroscopy (XPS) (**Figure 2a**) gives two typical Co $2p_{3/2}$ and $2p_{1/2}$ peaks at 778.3 and 794.2 eV from metallic Co,[41] respectively. Raman spectroscopy shows no clear Co-O peaks (**Figure S3**),[42] indicating that the *hcp* Co NSs are in a pure metallic state with no obvious surface oxidation. The extended X-ray absorption fine structure spectroscopy (EXAFS) of both *hcp* Co NS and commercial Co foil (**Figure 2b**, original data, no phase correction) shows that the NSs have a Co-Co bond peak at 2.2 Å, which is close to Co-Co lattice parameter in the *ab* plane of the *hcp* Co structure. Further analysis of the EXAFS wavelet transforms (WT) (**Figure 2c**) reveals that both NS and commercial Co foil have a similar intensity maximum at about 7.9 $Å^{-1}$, which is attributed to *hcp* Co-Co on the metallic Co surface. The best fitting analysis (**Figure 2d**, **Figure S4**, **S5** and **Table S1**) confirms that the main peak originates from the Co-Co first-shell coordination with the *hcp* Co coordination number (6.53) much smaller than the commercial bulk Co foil one (11.88). Compared to the bulk structure, the ultrathin *hcp* Co NSs have much more under-coordinated Co atoms due to the largely exposed surface, which is important for enhancing their catalysis for CO_2RR. We also measured the magnetic properties of these NSs at room temperature (**Figure 2e**). The NSs are ferromagnetic with their saturated magnetic moment reaching 154 emu g^{-1}, close to the bulk Co value (~162 emu g^{-1}).[43]

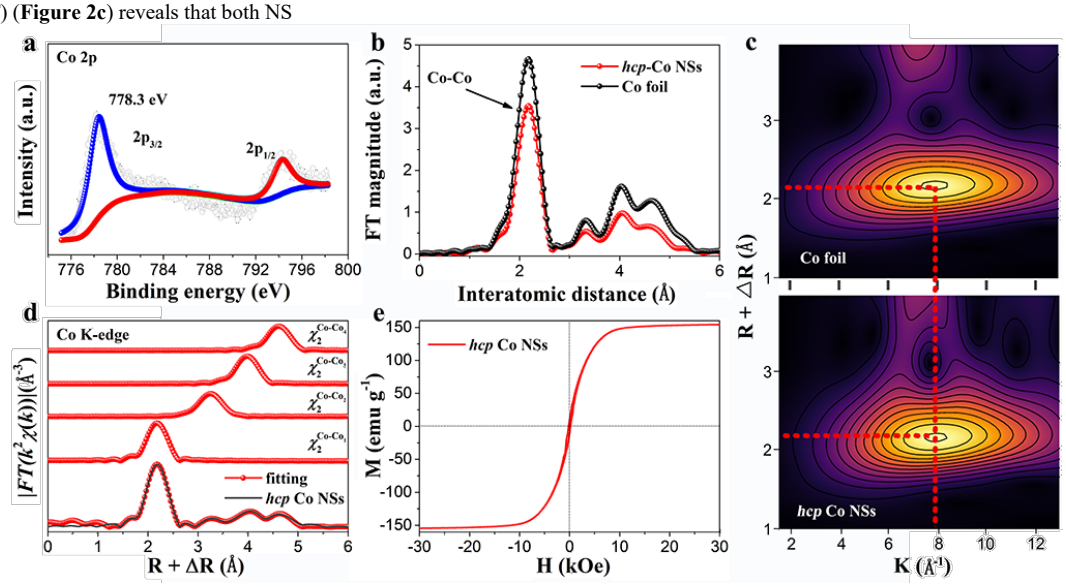

Figure 2. Surface, electronic and magnetic properties of the *hcp* Co NSs. (a) Co 2p XPS spectra of the *hcp* Co NSs. (b) EXAFS spectra of Co K-edge at R-space for *hcp* Co NSs and commercial Co foil. (c) Wavelet transforms for the k^3-weighted Co K-edge EXAFS signals of *hcp* Co NSs and commercial Co foil. (d) Co K-edge EXAFS of *hcp* Co NSs in R spaces, where curves from top to bottom are only the Co-Co backscattering signals (χ_2) included in the fit and total signal is superimposed on the experimental signal. (e) Magnetic hysteresis loop of the *hcp* Co NSs measured at room temperature.

Electrocatalysis for CO_2RR. The *hcp* Co NSs were tested as the catalyst for CO_2RR in an aqueous solution of 0.5 M $KHCO_3$ (all potentials were first measured against the Ag/AgCl reference electrode, and were then converted to RHE (see details in SI and **Figure S6**). The cyclic voltammetry (CV) studies (**Figure 3a**) indicate that the *hcp* Co NSs have no reduction peak in the negative reduction potential under Ar, suggesting that the Co NSs have no detectable surface oxides present (The Co NSs can be oxidized at 0.5 V). The CV curve under CO_2 has an apparent reduction peak at -0.4 V, which

is attributed to the Co-catalyzed reduction of CO_2, and the presence of CO_2 also promotes Co oxidation at 0.45 V due to the CO_2-induced decrease in pH value of the electrolyte solution. Under a continuous CO_2 flow condition, the electrochemical CO_2RR was studied at different reduction potentials and different times (**Figure S7**). From -0.2 V to -1.0 V, the *hcp* Co NSs reduced CO_2 to ethanal, ethanol, and methanol with H_2 as a by-product (**Figure 3b**), as characterized by gas chromatography (**Figure S8**), ^{1}H-NMR (**Figure S9**), and mass spectroscopy (MS) (**Figure S10**) (the representative calibration plots that were used to quantify each product are also given in **Figure S11 and S12**). Studying more potential-dependent CO_2RR from -0.05 to -0.2 V, we detected (by ^{1}HNMR) ethanal, ethanol and methanol from the electrolyte at -0.12 V (**Figure S13**), suggesting that the onset reduction potential for the *hcp* Co NS-catalyzed CO_2RR is around -0.1 V. At -0.4 V, the FE for ethanal reached 60%, while at the same reduction potential, FEs for ethanol and methanol were at 10% and 12%, respectively. Studying the ^{1}H-NMR spectrum of ethanal, we noticed that the CH_3 doublet peak appears at 2.12 ppm as expected, and also at 1.06 ppm. We performed a controlled ethanal/ethanol concentration-dependent NMR experiment in the 0.5 M $KHCO_3$ solution. We found that at a volume concentration of 1/500 ($(V_{ethanol} + V_{ethanal})/V_{solution}$), the ethanal-$CH_3$ doublet shows up at 2.12 ppm, but its hydrated form ($CH_3CH(OH)_2$) is also clearly visible with the hydrated ethanal-CH_3 peak appearing at 1.2 ppm (**Figure S14a**). At a volume concentration of 1/25000, the ethanal-CH_3 doublet shifts from 2.12 ppm to 1.06 ppm and mixes with ethanol-CH_3 (**Figure S14b**). Our further ^{1}H-NMR studies showed that the 10 μL ethanal/10 μL ethanol sample (**Figure S14c**, **d**) has a very weak peak at 9.55 ppm due to the obvious –CHO hydration in the mixed aqueous solution to $–CH(OH)_2$. As a comparison, the 100 μL ethanal/10 μL ethanol sample (**Figure S14e**, **f**) shows a much stronger peak at 9.55 ppm. These control experiments further support what we concluded from the ^{1}H-NMR analysis of the CO_2RR products that both ethanal and ethanol are obtained from the reduction reaction, and ethanal and its hydrated form co-exist in the electrolyte solution.

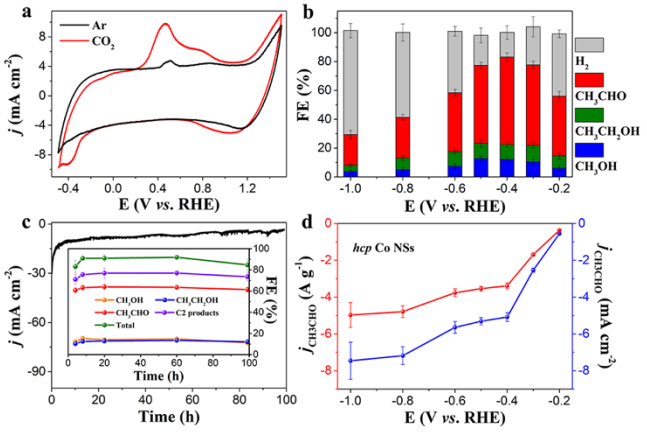

Figure 3. Catalytic performance of *hcp* Co NSs for CO_2RR. (a) CV curves of *hcp* Co NSs in Ar or CO_2 atmosphere. (b) Reduction potential-dependent FE of electrochemical CO_2RR catalyzed by *hcp* Co NSs. (c) Reduction current change and product FE (inset) over time during continuous electrochemical CO_2RR catalyzed by *hcp* Co NSs. (d) Reduction potential dependent mass activity (red) and *j* (blue) for the formation of CH_3CHO.

To prove that ethanal, ethanol, and methanol were indeed generated from CO_2RR, we tested CO_2RR in the 0.1 M Na_2SO_4 solution (to eliminate the $KHCO_3$ effect), and $^{13}CO_2$RR in the 0.5 M $KHCO_3$ solution under the same catalytic condition. As shown in ^{1}H-NMR (**Figure S15a, b**), ^{13}C-NMR (**Figure S15c**), and MS spectra (**Figure S15d**), ethanal (and its hydrated form), ethanol and methanol are present in the electrolyte. The ethanal-CH_3 peaks at ~2.1 ppm (more easily visible than those from its hydrated form at ~1.1 ppm where they overlap with ethanol-CH_3) show the expected ethanal-CH_3 doublet splitting caused by ^{1}H-^{13}C coupling (**Figure S15b**), confirming the formation of ethanal-$^{13}CH_3$ from the $^{13}CO_2$RR. Meanwhile, the satellite peaks induced by the ^{13}C are also noted near 1.2 ppm next to the triplet peak. The MS spectra clearly demonstrate the [M-H] peaks of the products of CH_3OH, CH_3CH_2OH and CH_3CHO, supporting the NMR results of the CO_2RR products (**Figure S15d**). Additionally, we tested the CO_2RR performance of the commercial Ketjen (KJ) carbon support and found no sign of the CO_2RR products (only trace of H_2 was detected from the reaction solution) (**Figure S16**), confirming that the observed catalytic CO_2RR originates from the *hcp* Co NSs, not from the carbon support. Furthermore, we analyzed the *hcp* Co NS sample with inductively coupled plasma-optical emission spectroscopy (ICP-OES) and found the sample before and after the CO_2RR test contained only Co, no Cu (**Table S2**). This proves that the observed CO_2RR catalysis is not from Cu, but from the *hcp* Co NSs. Compared with the Co- and Cu-based CO_2RR catalysts reported recently (**Table S3**), our *hcp* Co NSs show the unique catalysis for the CO_2 conversion to CH_3CHO (60% FE) with the total FE to C-products reaching 82%.

The *hcp* Co NSs were not only active and selective for the CO_2RR, but also stable in the CO_2RR condition as the FE of each product (**Figure 3c**), as well as the NS morphology/structure (**Figure S17**), Co binding properties (**Figure S18** and **S19**), and magnetic performance (**Figure S20**) remained nearly unchanged in the 100 h electrolysis period at -0.4 V. We should note here that although the morphology and crystal structure of the Co NSs are well-maintained during the 100 h electrolysis, the CO_2 concentration on the catalyst surface may be decreasing due to the near-catalyst-surface pH change and the CO_2 diffusion restriction, which causes the slight drop of the overall current density (*j*) (inset in **Figure 3c**). The reduction potential dependent ethanal selectivity peaks at -0.4 V, where its FE reaches 60% (**Figure 3b**) with *j* of 5.1 mA cm^{-2} and mass activity of 3.4 A g^{-1} (**Figure 3d**). At more negative potentials, both the reduction *j* and mass activity increase (**Figure 3d**), but the ethanal formation FE decreases (**Figure 3b**) due to the competition with the hydrogen evolution reaction (HER). Re-plotting the potential-dependent *j* and mass activity (**Figure 3d**) in the logarithmic scale, we obtained two linear relations (**Figure S21**), suggesting that the CO_2RR is dominated by the electrochemical process.

Further, we studied how the structure change affects the CO_2RR performance of Co NSs. The *hcp* Co NSs are structurally more stable and 500 °C annealing did not convert the structure to *fcc*, rather to the mixed *hcp*/*fcc* (**Figure S22**). The *fcc* Co NSs were obtained when the *hcp* Co NSs were annealed at 900 °C in H_2/Ar for 3 h. The TEM image shows that the annealed sample still has a nanosheet morphology (**Figure S23**). The XRD pattern supports the structure conversion from *hcp* to *fcc* (**Figure S24a**) and XPS confirms that the NS surface is dominated by metallic Co peaks (**Figure S24b**). The *hcp* to *fcc* conversion did not change the NS magnetic property as the *fcc* Co NSs are still ferromagnetic with magnetic moment reaching 148 emu g^{-1} (**Figure S25**), comparable to the *hcp* Co NSs. When the *fcc* Co NSs were tested for CO_2RR at -0.4 V, only H_2 was detected. At -1.0 V, the catalysis yielded a mixture of CH_4 (16% FE), C_2H_4 (10% FE) and CH_3CHO (8% FE) (**Figure S26**). This suggests that the *fcc* Co NS surface is much less active than the *hcp* Co NS one for the CO_2RR, and at the more negative reduction potential (-1.0 V), the *fcc* Co NSs tend to catalyze the CO_2RR to deep hydrogenation products (CH_4 and C_2H_4). We further prepared *fcc* Co NPs (see details in SI, **Figure S27a**) and studied their CO_2RR. We found that these NPs only catalyzed the CO_2RR to formate (12% FE at -0.6 V and 25% FE at -1.0 V) (**Figure S27b**). Compared with three different Co-catalysts we studied here, we can see that the NS morphology is necessary for C-C coupling and that the *hcp* Co arrangement is key for the selective CO_2RR to CH_3CHO.

Insights of the Co NS-catalyzed CO_2RR. To understand the high performance of *hcp* Co NSs in catalysing CO_2RR to CH_3CHO, we first performed ultraviolet photoelectron spectroscopy (UPS) of the NS samples to obtain the valence band energies (EV) of the *hcp* and *fcc* Co NSs, and then the DFT calculations to investigate the CO_2RR on *hcp* and *fcc* Co NSs. As shown in **Figure S28**, the E_V of *hcp* and *fcc* Co NSs was calculated to be 7.28 and 7.92 eV by subtracting the width of the He I UPS spectra from the excitation energy (21.22 eV). From the electronic perspective, the change of Co arrangement from -ABAB- pattern in the *hcp* Co to -ABCABC- one in the *fcc* Co noticeably varies their bonding and anti-bonding orbital distributions near the Fermi level (E_F), in which the *hcp* Co demonstrates more electron-rich feature than the *fcc* Co for promoting the CO_2RR (**Figure 4a**, **b** and **Figure S29a**, **b**). Notably, the band structure of *hcp* Co NSs displays an intense electronic distribution near E_F, leading to an efficient electron transfer process (**Figure 4c**) that is beneficial for CO_2 reduction. In comparison, the *fcc* Co NSs show a larger energy gap between CB and VB (**Figure 4d**), which is induced by the high electron repulsive energy originated from the higher electron concentration near the *fcc* Co surface. Owing to the small structural difference within two different Co NS structures, the spin state is introduced to unravel the electronic structure variation induced by the spin polarization. The projected partial density of states (PDOS) confirm that the *hcp* Co is strongly spin-polarized, in which the polarized d-band of Co-3d orbitals apparently crosses E_F. This is attributed to the alleviation of the repulsive energy of more empty bands due to the splitting of spin-polarized orbitals, which indicates that the subtle atomic arrangement difference between the *hcp* and *fcc* Co leads to the quite obvious change in the local electronic environment on the Co-3d orbitals. The rich electronic

environment on the Co-3d of the *hcp* Co (**Figure 4e**) is beneficial in promoting CO-CO coupling.[44] For the *fcc* Co, the spin-polarization becomes much weaker, and the occupied d-bands of Co still locate below E_F, creating a barrier for electron transfer (**Figure 4f**). In contrast, without the consideration of spin polarization, the PDOS of *hcp* and *fcc* Co only display a subtle peak shifting, which cannot reveal the intrinsic difference of electronic environments (**Figure S29c**).

From the chemisorption point of view, the limited p-d overlapping supports the appropriate adsorption strength of C-species. The pinned bands of intermediates species near E_V-4.0 eV are noted (E_V = 0 for EF) (**Figure 4g**), demonstrating optimal preservation of electroactivity of the *hcp* Co surface during CO_2RR. On the *fcc* Co surface, however, a novel linear correlation regarding the dominant orbital peaks of key intermediates suggests the fast electron transfers towards the C_1 pathway (**Figure 4h**). The Co surface electronic structure also changes slightly upon the adsorption of H_2O, CO and H (**Figure S29d**, **e**), suggesting a possible competitive HER pathway. Through the reciprocal phonon dispersion, we also innovatively reflect the stronger surface oscillation of *fcc* Co based on the two "Camel Hump" along M→L and H→K path in optical branches, which is evidently stronger than that on the *hcp* Co. This high frequency of phonon oscillation (large vibration energy) on the *fcc* Co limits the C-C coupling pathway that is often determined by less constrained electron transfer (**Figure 4i**).

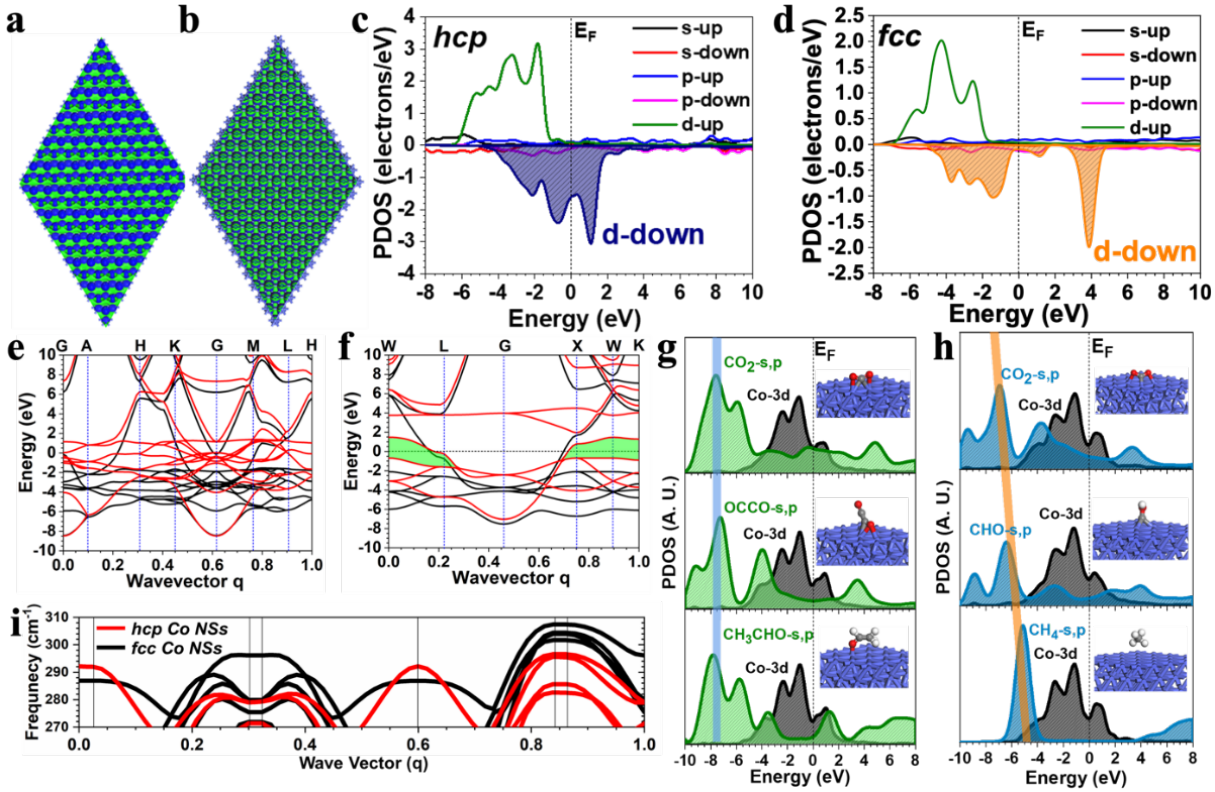

Figure 4. Electronic structure of Co NSs for CO_2RR. The real spatial orbital distribution of the bonding and anti-bonding near E_F of (a) *hcp* NSs and (b) *fcc* Co NSs. The Band structure of (c) *hcp* Co NSs and (d) *fcc* Co NSs. The green region represents the gap for inter-layer electron transfer on the surfaces. The PDOS of (e) *hcp* Co NSs and (f) *fcc* Co NSs. PDOS of key intermediates adsorption on (g) *hcp* Co NSs and (h) *fcc* Co NSs. (i) The partial phonon dispersion of *hcp* Co NSs and *fcc* Co NSs.

The unique surface phonon oscillation frequencies on these Co NS surfaces determine the reactant adsorption energies (**Figure 5a**, **b**). On the *hcp* Co surface, the CO_2 adsorption energies are limited in a small range (1.610-1.617 eV) (**Figure 5a** left), confirming that this surface is an evenly electro-activated surface with more exposed active sites. On the contrary, the *fcc* surface shows a regulated adsorption energy mapping with a nearly linear change (**Figure 5a** right), indicating strongly preferred active sites, which can lead to the activation of CO_2 to C_1 products. The adsorption strength of H_2O shows limited ranges over both surfaces, in which the adsorption of *hcp* surface is slightly stronger to facilitate the CO_2RR (**Figure 5b**). The adsorption energy mappings indicate the interruption of the linear correlation is pivotal to redirect the CO_2RR to the C_2 routes. We further plotted the energetic reaction pathway to supply a comprehensive understanding of the CO_2RR process based on the well-accepted proposed mechanisms.[45] The adsorption structures of all reaction intermediates are listed in **Figure S30**, **S31** and the corresponding energies of the reaction pathways on *hcp* and *fcc* Co NSs are listed in **Table S4** and **S5**. Due to the complexity of the CO_2RR process, the solvation effects are not included in our calculations, but this does not invalidate our calculations as previous studies have shown that the solvation terms do not impact the accurate descriptions of the electronic structure and energetic trend.[46,47] On the *hcp* surface, the C_2 pathway towards CH_3CHO shows an overall energy release of -1.32 eV while other competitive pathways to form C_2H_4, CH_3OH and CH_3CH_2OH are suppressed by the much higher energy barriers, which is consistent with the high FE of CH_3CHO generation (**Figure 5c**). The CO_2RR process on the *fcc* Co surface meets more energy barriers, leading to a lower electrocatalysis efficiency and limited FE. Although the reaction barrier leading to the formation of CH_3CH_2OH is higher than CH_3CHO, it is thermodynamically possible to reduce CH_3CHO to CH_3CH_2OH, which explains why experimentally CH_3CH_2OH was detected as a minor product (10% FE) compared to CH_3CHO (60% FE). On the *fcc* Co NS surface, the energy cost of forming [CHO]* is slightly lower than that of [OCCO]* and further spontaneous hydrogenation can lead to the formation of CH_4 (**Figure 5d**). Our calculations further show that the C-C coupling is dependent on the CO dimer distance on the Co NS surface. The *hcp* Co NS shows an efficiency superior to the *fcc* Co NS in forming C_2 products due to the evident energy preference (**Figure S29f**). We further considered the competitive HER in terms of H and CO binding energies.[44,48] The CO binding is preferred on the *hcp* Co NS surface, leading to the suppression of the HER. On the contrary, the H binding is more energetically favoured on the *fcc* Co NS surface, which suppresses CO_2RR at the less negative potential (**Figure S29g**, **h**). Therefore, theoretical calculations confirm that the subtle difference in the electronic structure of Co NSs (**Figure S32**) is of pivotal significance in determining the selectivity of the CO_2RR process.

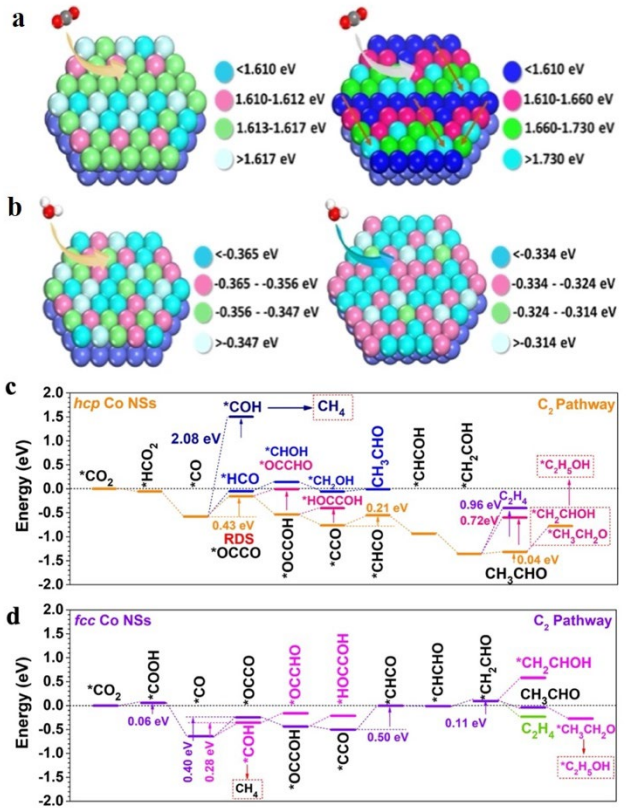

Figure 5. Energetic investigation of CO_2RR on *hcp* and *fcc* Co NSs. (a) Adsorption energy mapping of CO_2 on *hcp* Co NSs (Left) and *fcc* Co NSs (Right). (b) Adsorption energy mapping of H_2O on *hcp* Co NSs (Left) and *fcc* Co NSs (Right). Energetic pathway of CO_2RR on (c) *hcp* Co NSs and (d) *fcc* Co NSs.

Conclusion:

In this work, we report a new transition metal catalyst based on *hcp* Co NSs for the selective CO_2RR to ethanal. Considering that the dominant catalysts that have been studied for the CO_2 reduction to hydrocarbons are Cu-based, our discovery of *hcp* Co NS catalyst is a significant advance, which presents a novel direction of designing efficient CO_2RR catalyst. Our current study shows that both NS morphology and *hcp* structure are key to the CO_2RR for the generation of ethanal (FE 60%, current density 5.1 mA cm^{-2} and mass activity 3.4 A g^{-1}) along with minor products of ethanol (FE 10%) and methanol (FE 12%). The superior CO_2RR performance of the *hcp* Co NS catalyst originates from its intra-layer electron transfer, facilitating the [OC-CO]* coupling and subsequent hydrogenation of the intermediates to form ethanal. Unlike Cu catalysts, our *hcp* Co NS catalyst is both chemically and thermally stable, offering a robust surface platform for investigating CO_2RR mechanisms, and for exploring the catalysis synergy with other CO_2RR catalysts to further improve CO_2 reduction activity and selectivity.

ASSOCIATED CONTENT

Supporting Information

This material is available free of charge via the Internet at http://pubs.acs.org. Additional experimental details, characterization, DFT calculation details, SEM, TGA, Raman, EXAFS, NMR, TEM, XPS, VSM, including Figures S1-S32 and Tables S1-S5.

AUTHOR INFORMATION

Corresponding Author

*bhuang@polyu.edu.hk
*xipx@lzu.edu.cn
*ssun@brown.edu

Author Contributions

[#]J.Y, Z.Y and J.J contributed equally.

Notes

The authors declare no competing financial interests.

ACKNOWLEDGMENT

The work was supported by the American Chemical Society Petroleum Research Fund (57114-ND5) and in part by the Center for the Capture and Conversion of CO_2, a Center for Chemical Innovation funded by the National Science Foundation, CHE-1240020. M.M. was supported by the National Science Foundation Graduate Research Fellowship, under Grant No. 1644760. This work also supported by the National Natural Science Foundation of China (NSFC) (Nos. 21931001 and 21922105), the Special Fund Project of Guiding Scientific and Technological Innovation Development of Gansu Province (2019ZX–04), and the 111 Project (B20027). We also acknowledge support by the Fundamental Research Funds for the Central Universities (lzujbky-2021-pd04, lzujbky-2021-sp41 and lzujbky-2021-it12). B.H. acknowledges the support of the Natural Science Foundation of China (NSFC) (No. 21771156) and the Early Career Scheme (ECS) fund (Grant PolyU 253026/16P) from the Research Grant Council (RGC) in Hong Kong. B.H. also thanks to the support from Research Institute for Smart Energy (RISE) in HK-PolyU. J.Y. acknowledges the support of the China Scholarship Council (NO. 201806180113), the support of the China Postdoctoral Science Foundation (2021M691375) and the China National Postdoctoral Program for Innovative Talents (BX20200157).

REFERENCES

(1) Appel, A. M.; Bercaw, J. E.; Bocarsly, A. B.; Dobbek, H.; DuBois, D. L.; Dupuis, M.; Ferry, J. G.; Fujita, E.; Hille, R.; Kenis, P. J. A.; Kerfeld, C. A.; Morris, R. H.; Peden, C. H. F.; Portis, A. R.; Ragsdale, S. W.; Rauchfuss, T. B.; Reek, J. N. H.; Seefeldt, L. C.; Thauer, R. K.; Waldrop, G. L. Frontiers, Opportunities, and Challenges in Biochemical and Chemical Catalysis of CO_2 Fixation. *Chem. Rev.* **2013**, *113*, 6621−6658.

(2) Diercks, C. S.; Liu, Y.; Cordova, K. E.; Yaghi, O. M. The role of reticular chemistry in the design of CO_2 reduction catalysts. *Nat. Mater.* **2018**, *17*, 301−307.

(3) Whipple, D. T.; Kenis, P. J. A. Prospects of CO_2 Utilization via Direct Heterogeneous Electrochemical Reduction. *J. Phys. Chem. Lett.* **2010**, *1*, 3451−3458.

(4) Nam, D. H.; Bushuyev, O. S.; Li, J.; De Luna, P.; Seifitokaldani, A.; Dinh, C. T.; Garcia de Arquer, F. P.; Wang, Y.; Liang, Z.; Proppe, A. H.; Tan, C. S.; Todorovic, P.; Shekhah, O.; Gabardo, C. M.; Jo, J. W.; Choi, J.; Choi, M. J.; Baek, S. W.; Kim, J.; Sinton, D.; Kelley, S. O.; Eddaoudi, M.; Sargent, E. H. Metal-Organic Frameworks Mediate Cu Coordination for Selective CO_2 Electroreduction. *J. Am. Chem. Soc.* **2018**, *140*, 11378−11386.

(5) Liu, M.; Pang, Y.; Zhang, B.; De Luna, P.; Voznyy, O.; Xu, J.; Zheng, X.; Dinh, C. T.; Fan, F.; Cao, C.; de Arquer, F. P.; Safaei, T. S.; Mepham, A.; Klinkova, A.; Kumacheva, E.; Filleter, T.; Sinton, D.; Kelley, S. O.; Sargent, E. H. Enhanced Electrocatalytic CO_2 Reduction via Field-induced Reagent Concentration. *Nature* **2016**, *537*, 382−386.

(6) Hod, I.; Sampson, M. D.; Deria, P.; Kubiak, C. P.; Farha, O. K.; Hupp, J. T. Fe-Porphyrin-Based Metal−Organic Framework Films as High-Surface Concentration, Heterogeneous Catalysts for Electrochemical Reduction of CO_2. *ACS Catal.* **2015**, *5*, 6302−6309.

(7) Li, C. W.; Ciston, J.; Kanan, M. W. Electroreduction of carbon monoxide to liquid fuel on oxide-derived nanocrystalline copper. *Nature* **2014**, *508*, 504−507.

(8) Jouny, M.; Luc, W.; Jiao, F. High-rate electroreduction of carbon monoxide to multi-carbon products. *Nat. Catal.* **2018**, *1*, 748−755.

(9) Bushuyev, O. S.; De Luna, P.; Dinh, C. T.; Tao, L.; Saur, G.; van de Lagemaat, J.; Kelley, S. O.; Sargent, E. H. What Should We Make with CO_2 and How Can We Make It? *Joule* **2018**, *2*, 825−832.

(10) Zhu, W.; Michalsky, R.; Metin, O.; Lv, H.; Guo, S.; Wright, C. J.; Sun, X.; Peterson, A. A.; Sun, S. Monodisperse Au Nanoparticles for Selective Electrocatalytic Reduction of CO_2 to CO. *J. Am. Chem. Soc.* **2013**, *135*, 16833−16836.

(11) Zhu, W.; Zhang, Y. J.; Zhang, H.; Lv, H.; Li, Q.; Michalsky, R.; Peterson, A. A.; Sun, S. Active and Selective Conversion of CO_2 to CO on Ultrathin Au Nanowires. *J. Am. Chem. Soc.* **2014**, *136*, 16132−16135.

(12) Geng, Z.; Kong, X.; Chen, W.; Su, H.; Liu, Y.; Cai, F.; Wang, G.; Zeng, J. Oxygen Vacancies in ZnO Nanosheets Enhance CO_2 Electrochemical Reduction to CO. *Angew. Chem., Int. Ed.* **2018**, *57*, 6054−6059.

(13) Klinkova, A.; De Luna, P.; Dinh, C.-T.; Voznyy, O.; Larin, E. M.; Kumacheva, E.; Sargent, E. H. Rational Design of Efficient Palladium Catalysts for Electroreduction of Carbon Dioxide to Formate. *ACS Catal*. **2016**, *6*, 8115−8120.

(14) Kang, P.; Cheng, C.; Chen, Z.; Schauer, C. K.; Meyer, T. J.; Brookhart, M. Selective electrocatalytic reduction of CO_2 to formate by water-stable iridium dihydride pincer complexes. *J. Am. Chem. Soc.* **2012**, *134*, 5500−5503.

(15) Li, X.; Li, L.; Liang, Y.; Sun, J.; Xu, X.; Jiao, X.; Xu, H.; Ju, Y.; Pan, J.; Zhu, Y. Xie, Ultrathin Conductor Enabling Efficient IR Light CO_2 Reduction. *J. Am. Chem. Soc.* **2019**, *141*, 423−430.

(16) Jiang, B.; Zhang, X.-G.; Jiang, K.; Wu, D.-Y.; Cai, W.-B. Boosting Formate Production in Electrocatalytic CO_2 Reduction over Wide Potential Window on Pd Surfaces. *J. Am. Chem. Soc.* **2018**, *140*, 2880−2889.

(17) Bassegoda, A.; Madden, C.; Wakerley, W. D.; Reisner, E.; Hirst, J. Reversible Interconversion of CO_2 and Formate by a Molybdenum-Containing Formate Dehydrogenase. *J. Am. Chem. Soc.* **2014**, *136*, 15473−15476.

(18) Ma, S.; Sadakiyo, M.; Heima, M.; Luo, R.; Haasch, R. T.; Gold, J. I.; Yamauchi, M.; Kenis, P. J. Electroreduction of Carbon Dioxide to Hydrocarbons Using Bimetallic Cu-Pd Catalysts with Different Mixing Patterns. *J. Am. Chem. Soc.* **2017**, *139*, 47−50.

(19) Loiudice, A.; Lobaccaro, P.; Kamali, A. E.; Thao, T.; Huang, H. B.; Ager, W. J.; Buonsanti, R. Tailoring Copper Nanocrystals towards C2 Products in Electrochemical CO_2 Reduction, *Angew. Chem., Int. Ed.* **2016**, *55*, 5789−5792.

(20) Kortlever, R.; Peters, I.; Balemans, C.; Kas, R.; Kwon, Y.; Mul, G.; Koper, M. T. Palladium-gold Catalyst for the Electrochemical Reduction of CO_2 to C1-C5 Hydrocarbons. *Chem. Commun*. **2016**, *52*, 10229−10232.

(21) Yu, S.; Wilson, J. A.; Heo, J.; Jain, K. P. Plasmonic Control of Multi-Electron Transfer and C–C Coupling in Visible-Light-Driven CO_2 Reduction on Au Nanoparticles. *Nano Lett.* **2018**, *18*, 2189−2194.

(22) Jung, H.; Lee, S. Y.; Lee, C. W.; Cho, M. K.; Won, D. H.; Kim, C.; Oh, H.-S.; Min, B. K.; Hwang, Y. J. Electrochemical Fragmentation of Cu_2O Nanoparticles Enhancing Selective C–C Coupling from CO_2 Reduction Reaction. *J. Am. Chem. Soc*. **2019**, *141*, 4624−4633.

(23) Kuhl, K. P.; Hatsukade, T.; Cave, E. R.; Abram, D. N.; Kibsgaard, J.; Jaramillo, T. F. Electrocatalytic Conversion of Carbon Dioxide to Methane and Methanol on Transition Metal Surfaces. *J. Am. Chem. Soc.* **2014**, *136*, 14107−14113.

(24) Li, Q.; Zhu, W.; Fu, J.; Zhang, H.; Wu, G.; Sun, S. Controlled assembly of Cu nanoparticles on pyridinic-N rich graphene for electrochemical reduction of CO_2 to ethylene. *Nano Energy* **2016**, *24*, 1−9.

(25) Reske, R.; Mistry, H.; Behafarid, F.; Cuenya, B. R.; Strasser, P. Particle Size Effects in the Catalytic Electroreduction of CO_2 on CuNanoparticles, *J. Am. Chem. Soc.* **2014**, *136*, 6978−6986.

(26) Raciti, D.; Cao, L.; J. T. Livi, K.; F. Rottmann, P.; Tang, X.; Li, C.; Hicks, Z.; H. Bowen, K.; J. Hemker, K.; Mueller, T.; Wang, C. Low-Overpotential Electroreduction of Carbon Monoxide Using Copper Nanowires. *ACS Catal*. **2017**, *7*, 4467−4472.

(27) Hori, Y.; Murata, A.; Takahashi, R.; Suzuki, S. Electroreduction of carbon monoxide to methane and ethylene at a copper electrode in aqueous solutions at ambient temperature and pressure. *J. Am. Chem. Soc.* **1987**, *109*, 5022−5023.

(28) Kim, J.; Choi, W.; Park, J. W.; Kim, C.; Kim, M.; Song, H. Branched Copper Oxide Nanoparticles Induce Highly Selective Ethylene Production by Electrochemical Carbon Dioxide Reduction. *J. Am. Chem. Soc.* **2019**, *141*, 6986−6994.

(29) Lee, S. Y.; Jung, H.; Kim, N.-K.; Oh, H.-S.; Min, B. K.; Hwang, Y. J. Mixed Copper States in Anodized Cu Electrocatalyst for Stable and Selective Ethylene Production from CO_2 Reduction. *J. Am. Chem. Soc*. **2018**, *140*, 8681−8689.

(30) Huang, J.; Mensi, M.; Oveisi, E.; Mantella, V.; Buonsanti, R. Structural Sensitivities in Bimetallic Catalysts for Electrochemical CO_2 Reduction Revealed by Ag–Cu Nanodimers. *J. Am. Chem. Soc*. **2019**, *141*, 2490−2499.

(31) Gao, D.; McCrum, T. I.; Deo, S.; Choi, Y.-W.; Scholten, F.; Wan, W.; Chen, G. J.; Janik, J. M.; Cuenya, B. R. Activity and Selectivity Control in CO_2 Electroreduction to Multicarbon Products over CuO_x Catalysts via Electrolyte Design. *ACS Catal.* **2018**, *8*, 10012−10020.

(32) Chang, Z.; Huo, S.; Zhang, W.; Fang, J.; Wang, H. The Tunable and Highly Selective Reduction Products on Ag@Cu Bimetallic Catalysts Toward CO_2 Electrochemical Reduction Reaction. *J. Phys. Chem. C* **2017**, *121*, 11368−11379.

(33) Deng, Y.; Huang, Y.; Ren, D.; Handoko, D. A.; She, Z. W.; Hirunsit, P.; Yeo, B. S. On the Role of Sulfur for the Selective Electrochemical Reduction of CO_2 to Formate on CuS_x Catalysts. *ACS Appl. Mater. Interfaces* **2018**, *10*, 28572−28581.

(34) Roberts, F. S.; Kuhl, P. K.; Nilsson, A. High Selectivity for Ethylene from Carbon Dioxide Reduction over Copper Nanocube Electrocatalysts. *Angew. Chem., Int. Ed.* **2015**, *54*, 5179−5182.

(35) Rahaman, M.; Dutta, A.; Zanetti, A.; Broekmann, P. Electrochemical Reduction of CO_2 into Multicarbon Alcohols on Activated Cu Mesh Catalysts: An Identical Location (IL) Study. *ACS Catal.* **2017**, *7*, 7946−7956.

(36) Handoko, D. A.; Chan, K. W.; Yeo, B. S. $-CH_3$ Mediated Pathway for the Electroreduction of CO_2 to Ethane and Ethanol on Thick Oxide-Derived Copper Catalysts at Low Overpotentials. *ACS Energy Lett*. **2017**, *2*, 2103−2109.

(37) O'Mara, B. P.; Wilde, P.; Benedetti, M. T.; Andronescu, C.; Cheong, S.; Gooding, J. J.; Tilley, D. R.; Schuhmann, W. Cascade Reactions in Nanozymes: Spatially Separated Active Sites inside Ag-Core–Porous-Cu-Shell Nanoparticles for Multistep Carbon Dioxide Reduction to Higher Organic Molecules. *J. Am. Chem. Soc*. **2019**, *141*, 14093−14097.

(38) Yang, H.; Wu, Y.; Li, G.; Lin, Q.; Hu, Q.; Zhang, Q.; Liu, J.; He, C. Scalable Production of Efficient Single-Atom Copper Decorated Carbon Membranes for CO_2 Electroreduction to Methanol. *J. Am. Chem. Soc*. **2019**, *141*, 12717−12723.

(39) Fu, J.; Zhu, W.; Chen, Y.; Yin, Z.; Li, Y.; Liu, J.; Zhang, H.; Zhu, J.-J.; Sun, S. Bipyridine-Assisted Assembly of Au Nanoparticles on Cu Nanowires to Enhance the Electrochemical Reduction of CO_2. *Angew. Chem., Int. Ed.* **2019**, *131*, 14238−14241.

(40) Chatterjee, T.; Boutin, E.; Robert, M. Manifesto for the routine use of NMR for the liquid product analysis of aqueous CO_2 reduction: from comprehensive chemical shift data to formaldehyde quantification in water. *Dalton Trans.* **2020**, *49*, 4257−4265.

(41) Wu, L.; Li, Q.; Wu, C. H.; Zhu, H.; Mendoza-Garcia, A.; Shen, B.; Guo, J.; Sun, S. Stable Cobalt Nanoparticles and Their Monolayer Array as an Efficient Electrocatalyst for Oxygen Evolution Reaction. *J. Am. Chem. Soc.* **2015**, *137*, 7071−7074.

(42) Gao, S.; Lin, Y.; Jiao, X.; Sun, Y.; Luo, Q.; Zhang, W.; Li, D.; Yang, J.; Xie, Y. Partially oxidized atomic cobalt layers for carbon dioxide electroreduction to liquid fuel. *Nature* **2016**, *529*, 68−71.

(43) Piao, M.; Zhang, Y.; Feng, S.; Zhang, H.; Zhang, F.; Chu, J.; Wang, X.; Zhang, Y.; Shi, H.; Li, C. Microwave plasma assisted reduction synthesis of hexagonal cobalt nanosheets with enhanced electromagnetic performances, *Nanotechnology* **2019**, *30*, 495601.

(44) Nitopi, S.; Bertheussen, E.; Scott, B. S.; Liu, X.; Engstfeld, K. A.; Horch, S.; Seger, B.; Stephens, E. L. I.; Chan, K.; Hahn, C.; K. Nørskov, J.; Jaramillo, F. T.; Chorkendorff, I. Progress and Perspectives of Electrochemical CO_2 Reduction on Copper in Aqueous Electrolyte, *Chem. Rev.* **2019**, *119*, 7610−7672.

(45) Ooka, H.; Figueiredo M. C.; Koper M. T. M. Competition between Hydrogen Evolution and Carbon Dioxide Reduction on Copper Electrodes in Mildly Acidic Media, *Langmuir*, **2017**, *33*, 9307−9313.

(46) Zhou, Y.; Che, F.; Liu, M.; Zou, C.; Liang, Z.; De, L. P.; Yuan, H.; Li J.; Wang, Z.; Xie, H.; Li, H.; Chen, P.; Bladt, E.; Quintero-Bermudez, R.; Sham, T.-K.; Bals, S.; Hofkens, J.; Sinton, D.; Chen, G.; Sargent E. H., Dopant-induced electron localization drives CO_2 reduction to C_2 hydrocarbons, *Nat. Chem*. **2018**, *10*, 974−980.

(47) Zhang, A.; Liang, Y.; Li, H.; Zhao, X.; Chen, Y.; Zhang, B.; Zhu, W.; Zeng, J. Harmonizing the Electronic Structures of the Adsorbate and Catalysts for Efficient CO_2 Reduction, *Nano Lett*. **2019**, *19*, 6547−6553.

(48) Peterson, A. A.; Abild-Pedersen, F.; Studt, F.; Rossmeisl, J.; Nørskov, K. J. How copper catalyzes the electroreduction of carbon dioxide into hydrocarbon fuels, *Energy Environ. Sci*. **2010**, *3*, 1311−1315.

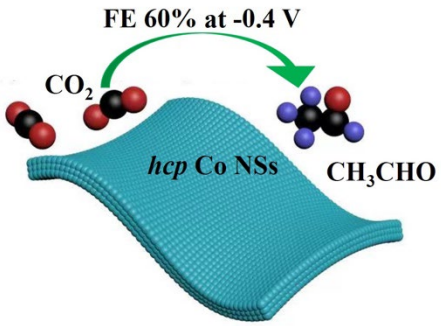

TOC